


Skyrmions and magnetic bubbles in spin-orbit coupled metallic magnets

Deepti Rana,¹ Soumyaranjan Dash¹,¹ Monika Bhakar,¹ Rajeshwari Roy Chowdhury,² Ravi Prakash Singh^{1,2},
Sanjeev Kumar,^{1,*} and Goutam Sheet^{1,†}

¹*Department of Physical Sciences, Indian Institute of Science Education and Research (IISER) Mohali,
Sector 81, S.A.S. Nagar, Manauli PO 140306, India*

²*Department of Physics, Indian Institute of Science Education and Research (IISER) Bhopal, PO 462066, India*

 (Received 14 June 2023; revised 22 October 2023; accepted 23 October 2023; published 20 November 2023)

Motivated by the observation of Skyrmion-like magnetic textures in two-dimensional (2D) itinerant ferromagnets Fe_nGeTe_2 ($n \geq 3$), we develop a microscopic model combining itinerant magnetism and spin-orbit coupling on a triangular lattice. The ground state of the model in the absence of magnetic field consists of filamentary magnetic domain walls revealing a striking similarity with our magnetic force microscopy experiments on Fe_3GeTe_2 . In the presence of magnetic field, these filaments were found to break into large-size magnetic bubbles in our experiments. We identify uniaxial magnetic anisotropy as an important parameter in the model that interpolates between magnetic Skyrmions and ferromagnetic bubbles. Consequently, our work uncovers new topological magnetic textures that merge properties of Skyrmions and ferromagnetic bubbles.

DOI: [10.1103/PhysRevB.108.184419](https://doi.org/10.1103/PhysRevB.108.184419)

I. INTRODUCTION

The topologically stable magnetic structures, such as the Skyrmions, are considered the building blocks of next-generation data storage and processing devices [1–8]. Consequently, identifying suitable magnetic materials that host such unusual magnetization textures has become a rapidly emerging area of research [9–19]. One of the key requirements for applications is the manipulation of such textures via ultralow electrical currents, and therefore it is desirable to have such magnetic textures realized in metallic magnets [11,12,20–25]. The appearance of isolated Skyrmions as well as Skyrmion lattices has been reported in thin films of a variety of chiral metallic magnets [12–15,26–33]. While a common understanding of magnetic Skyrmions in metals relies heavily on either a suitable free-energy functional in a continuum or classical spin models on lattices [8,34–39], more recently the importance of microscopic Hamiltonian-based understanding of Skyrmion formation has been recognized [40–43]. The latter approach allows for a finer distinction between ferromagnetic bubbles and Skyrmions, thereby providing a tunable control on the stability of different topological textures.

Motivated by the recent observation of metallic ferromagnetism in the van der Waals (vdW) magnets Fe_nGeTe_2 with $n = 3, 4, 5$ [44–46], we extend and investigate a recently proposed microscopic model for the broad class of vdW magnets. The model combines the effects of itinerant magnetism, spin-orbit coupling, and uniaxial anisotropy [40]. Starting from the microscopic electronic Hamiltonian on a triangular lattice, we derive an effective spin model. We explicitly demonstrate via large-scale Monte Carlo (MC) simulations, that the

ground state of the model consists of filamentary domain wall structures which show agreement with the magnetic force microscopy (MFM) images on high-quality single crystals of Fe_3GeTe_2 . However, the MFM images in the presence of an external magnetic field deviate from the in-field calculations within the model. We show that the inclusion of a uniaxial anisotropy term in the Hamiltonian allows for a consistent description of the results at zero and finite magnetic fields. Furthermore, we identify the easy-axis anisotropy as an important tuning parameter for the relative stability of different types of topological structures in spin-orbit coupled itinerant magnets.

II. THEORETICAL MODEL

In metallic magnets that consist of large magnetic moments and spin-orbit coupling (SOC), a generic starting model is the ferromagnetic Kondo lattice model (FKLM) in the presence of a Rashba term. We consider the Hamiltonian on a triangular lattice as

$$H = -t \sum_{i,\gamma,\sigma} (c_{i,\sigma}^\dagger c_{i+\gamma,\sigma} + \text{H.c.}) - J_H \sum_i \mathbf{S}_i \cdot \mathbf{s}_i - i\lambda \sum_{i,\gamma,\sigma\sigma'} c_{i\sigma}^\dagger [\boldsymbol{\tau} \cdot (\hat{\gamma} \times \hat{\mathbf{z}})]_{\sigma\sigma'} c_{j\sigma'} - h_z \sum_i S_i^z. \quad (1)$$

The annihilation (creation) operators $c_{i\sigma}$ ($c_{i\sigma}^\dagger$) satisfy the usual Fermion algebra. J_H (λ) denotes the strength of Kondo (Rashba) coupling, t is the nearest-neighbor hopping parameter on triangular lattice. $\boldsymbol{\tau}$ is a vector operator with the three Pauli matrices as components. \mathbf{s}_i (\mathbf{S}_i) denotes the electronic spin operator (localized classical spin) at site i . Assuming the lattice constant to be unity, $\hat{\gamma} \in \{\mathbf{a}_1, \mathbf{a}_2, \mathbf{a}_3\}$ are the primitive vectors of the triangular Bravais lattice with $\mathbf{a}_1=(1,0)$, $\mathbf{a}_2=(1/2,\sqrt{3}/2)$ and $\mathbf{a}_3=(-1/2,\sqrt{3}/2)$. The last term in Eq. (1) represents the Zeeman coupling of local moments to

*sanjeev@iisermohali.ac.in

†Also at S. N. Bose National Center for Basics Sciences, Salt Lake, JD Block, Sector III, Bidhannagar, West Bengal 700106, Kolkata; goutam@iisermohali.ac.in

an external magnetic field of strength h_z . $t = 1$ sets the basic energy unit in the model. Presence of Skyrmion Hall effect in the vdW magnets indicates that the strong coupling limit is more relevant as compared to the weak-coupling Ruderman-Kittel-Kasuya-Yoshida (RKKY) limit [47–50]. This leads to the Rashba double-exchange (RDE) Hamiltonian on a triangular lattice [40]

$$H_{\text{RDE}} = \sum_{(ij),\gamma} [g_{ij}^\gamma d_i^\dagger d_j + \text{H.c.}] - h_z \sum_i S_i^z, \quad (2)$$

where, $d_i(d_i^\dagger)$ annihilates (creates) an electron at site i with spin parallel to the localized spin. Site $j = i + \gamma$ is the nearest neighbor (nn) of site i along one of the three symmetry directions on the triangular lattice. The projected hopping g_{ij}^γ depend on the orientations of the local moments \mathbf{S}_i and \mathbf{S}_j . The tight-binding t_{ij}^γ and Rashba λ_{ij}^γ contributions to $g_{ij}^\gamma = t_{ij}^\gamma + \lambda_{ij}^\gamma$ are given by [40]

$$\begin{aligned} t_{ij}^\gamma &= -t \left[\cos\left(\frac{\theta_i}{2}\right) \cos\left(\frac{\theta_j}{2}\right) + \sin\left(\frac{\theta_i}{2}\right) \sin\left(\frac{\theta_j}{2}\right) e^{-i(\phi_i - \phi_j)} \right], \\ \lambda_{ij}^{\mathbf{a}_1} &= \lambda_{ij}^x, \quad \lambda_{ij}^{\mathbf{a}_{2/3}} = \pm \frac{1}{2} \lambda_{ij}^x + \frac{\sqrt{3}}{2} \lambda_{ij}^y, \\ \lambda_{ij}^x &= \lambda \left[\sin\left(\frac{\theta_i}{2}\right) \cos\left(\frac{\theta_j}{2}\right) e^{-i\phi_i} - \cos\left(\frac{\theta_i}{2}\right) \sin\left(\frac{\theta_j}{2}\right) e^{i\phi_j} \right], \\ \lambda_{ij}^y &= i\lambda \left[\sin\left(\frac{\theta_i}{2}\right) \cos\left(\frac{\theta_j}{2}\right) e^{-i\phi_i} + \cos\left(\frac{\theta_i}{2}\right) \sin\left(\frac{\theta_j}{2}\right) e^{i\phi_j} \right], \end{aligned} \quad (3)$$

where θ_i (ϕ_i) is the polar (azimuthal) angle for localized moment \mathbf{S}_i .

The Hamiltonian Eq. (2) describes a modified tight-binding model where the hopping integrals are dependent on the configuration of classical spins. Therefore, the energy of the system depends on the classical spin configurations. This dependence can be formally written as an effective spin Hamiltonian by following a procedure well known for double-exchange models [40,51]. For the present case of Rashba coupling on a triangular lattice, we obtain

$$\begin{aligned} H_{\text{eff}} &= - \sum_{(ij),\gamma} D_{ij}^\gamma f_{ij}^\gamma - h_z \sum_i S_i^z, \\ \sqrt{2} f_{ij}^\gamma &= [t^2(1 + \mathbf{S}_i \cdot \mathbf{S}_j) + 2t\lambda\hat{\gamma}' \cdot (\mathbf{S}_i \times \mathbf{S}_j) \\ &\quad + \lambda^2(1 - \mathbf{S}_i \cdot \mathbf{S}_j + 2(\hat{\gamma}' \cdot \mathbf{S}_i)(\hat{\gamma}' \cdot \mathbf{S}_j))]^{1/2}, \\ D_{ij}^\gamma &= \langle [e^{ih_{ij}^\gamma} d_i^\dagger d_j + \text{H.c.}] \rangle_{\text{gs}}. \end{aligned} \quad (4)$$

In the above, f_{ij}^γ (h_{ij}^γ) is the modulus (argument) of complex number g_{ij}^γ , and $\langle \hat{O} \rangle_{\text{gs}}$ denotes expectation values of operator \hat{O} in the ground state. Assuming constant coupling parameters has been shown to be a good approximation for studying ground-state phases of H_{eff} [40], therefore we set $D_{ij}^\gamma \equiv D_0 = 1/\sqrt{2}$ to study H_{eff} . We perform Monte Carlo (MC) simulations on Hamiltonian Eq. (4) via the standard Markov chain MC using Metropolis algorithm. We begin the simulations at high temperature and reduce temperature in small steps, using 10^5 MC steps for equilibration at each temperature. The magnetic field value is kept zero during

this cooling process. Finally, at low but finite temperature we increase magnetic field in step-wise manner. Once again 10^5 MC steps for equilibration are used at each magnetic field value, followed by an equal number of steps for recording averages of observables. Most importantly, the MC approach allows access to full spatial details that can be used not only to identify unusual magnetization textures but also to compare with spatially resolved experimental data as will be discussed later. Therefore, our analysis focuses on the typical spin configurations obtained at low temperatures and their evolution with applied magnetic field. We also compute the spin structure factor $S(\mathbf{q})$ in order to identify the presence of ordered magnetic phases. The spin structure factor (SSF) is given by $S(\mathbf{q}) = \frac{1}{N^2} \langle \sum_{i,j} \mathbf{S}_i \cdot \mathbf{S}_j \exp[-i(\mathbf{r}_i - \mathbf{r}_j) \cdot \mathbf{q}] \rangle$, where N is the number of sites, and the angular bracket denotes averaging over MC configurations.

The low-temperature magnetic states, with varying strengths of SOC, are shown in Fig. 1. For small to intermediate values of λ/t , we find the filamentary domain structure of spins [see Figs. 1(a)–1(b)]. The thickness of these domains decreases with the increasing strength of SOC. For a sufficiently large lattice size, we find that the filaments are oriented along all possible directions, and this is more clearly reflected in the structure factor plots where a circular pattern in the $S(\mathbf{q})$ is obtained [see Figs. 1(d)–1(e)]. This freedom of the domains to orient freely in any direction is a consequence of the anisotropic Dzyaloshinskii-Moriya (DM) interaction encoded in the linear λ term in the f_{ij} in Hamiltonian Eq. (4). For larger values of λ/t , we obtain a spin-spiral state with a single-ordering wavevector [see Figs. 1(c) and 1(f)]. The origin of this state is related to the importance of the λ^2 term in the effective Hamiltonian. Note that the λ^2 term prefers Ising-like interactions of different components along different directions, leading to a classical Kitaev model with degenerate ground states. Therefore, there are three states, related by the rotational symmetry of the triangular lattice, that can be realized as ground states. In terms of the SSF, the symmetry-related states will display a SSF that is already rotated by $2\pi/3$ and $4\pi/3$ with respect to Fig. 1(f). Note that the λ^2 term resembles a truncated dipolar interaction term. Therefore, similar magnetic domains are likely to be present in any simulation that includes dipolar interactions [52].

III. EXPERIMENTS

A. Crystal growth and characterization

Now, we focus on the experimentally observed magnetic domain structures on Fe_3GeTe_2 where the characteristic features of the model, namely the existence of ferromagnetism [53], metallicity [44], and high spin-orbit coupling [54] exist naturally. Fe_3GeTe_2 is a van der Waals layered material exhibiting a hexagonal lattice structure with space-group $P6_3/mmc$. It is an itinerant ferromagnet with a Curie temperature ranging from 220–230 K in bulk [53,55]. High-quality single crystals of Fe_3GeTe_2 , synthesized by chemical vapor transport, were used for our magnetic force microscopic (MFM) measurements. A stoichiometric mixture of the ingredients elements [Fe (3N), Ge (3N), and Te (3N)] in the powder form was sealed in an evacuated quartz tube along with I_2 as

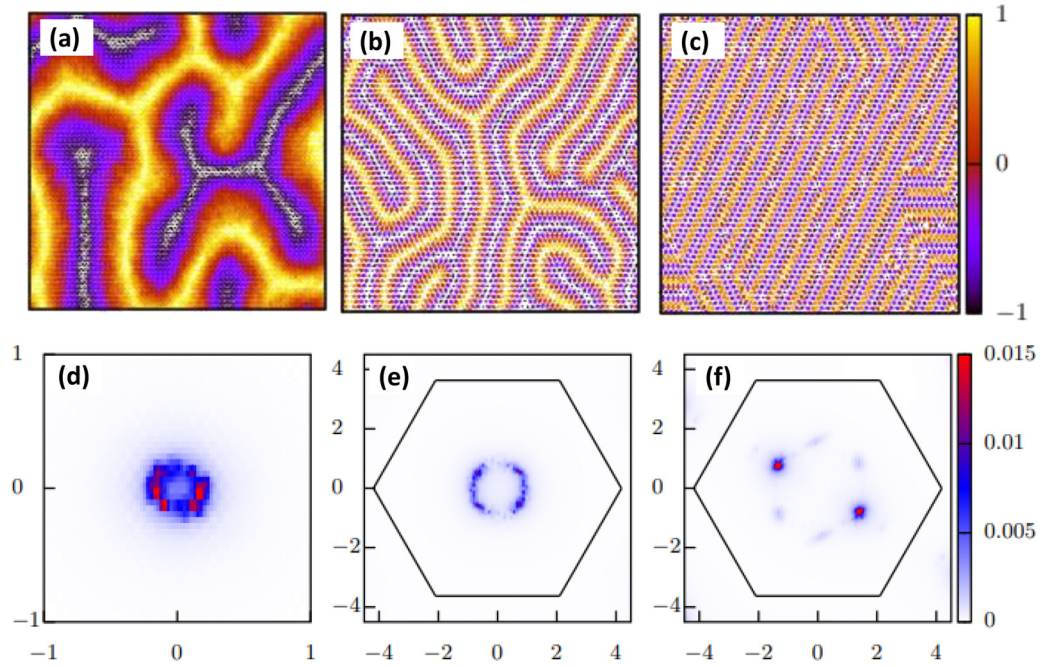


FIG. 1. Real-space view of spin configurations at low temperature ($T/t = 0.01$) for (a) $\lambda/t = 0.1$, (b) $\lambda/t = 0.5$, and (c) $\lambda/t = 1$. The color bar corresponds to the z component, and the arrows indicate the planar components of the spins. (d)–(f) The corresponding spin structure factors for the three values of the SOC strength λ/t .

the transport agent. The tube was kept in a two-zone furnace at a temperature gradient of $750^\circ\text{C}/650^\circ\text{C}$. Platelike single crystals were obtained after two weeks. Figure 2(a) shows the optical microscope image of a single crystal of Fe_3GeTe_2 . Figure 2(b) shows the experimental out-of-plane x-ray diffraction (XRD) results for the single crystal where sharp peaks were observed. The observed Bragg peaks can be indexed with $(00l)$ peaks. Figure 2(c) shows the Laue diffraction pat-

tern of a Fe_3GeTe_2 crystal, confirming the sixfold symmetry of the hexagonal structure and high crystallinity of the grown sample. The chemical composition of the grown crystals was confirmed from atomic percentage ratios obtained from energy-dispersive x-ray (EDX) spectroscopy measurements within the instrumental limit [Figure 2(d)]. Further characterization details of the sample are reported elsewhere [56].

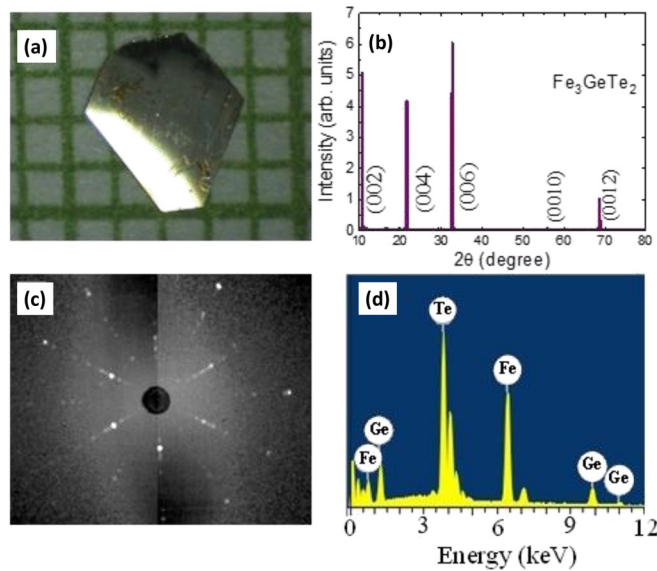


FIG. 2. (a) Optical micrograph of single crystal of Fe_3GeTe_2 utilized in the measurements. (b) Out-of-plane x-ray diffraction pattern of Fe_3GeTe_2 at room temperature. (c) Laue diffraction pattern obtained on Fe_3GeTe_2 single crystal. (d) EDX spectra for Fe_3GeTe_2 .

B. MFM results and their comparison with the theoretical model

We imaged the magnetic domains in Fe_3GeTe_2 by magnetic force microscopy (MFM) performed at different temperatures and under magnetic fields. In magnetic force microscopy (MFM), a silicon cantilever/tip coated with a magnetic coating (typically Co or Al) is used along with an interferometer-based detection system to probe the local magnetic properties of the sample by measuring the magnetic interactions between the tip and the sample. A low-temperature compatible magnetic force microscope (Attocube LT-MFM), working down to 1.6 K, equipped with a single-mode fiber-based interferometer was used for performing the ferromagnetic domain imaging on the ferromagnet. The phase images presented in this work were obtained in dual-pass mode, also known as lift mode. In the single pass, the cantilever using a feedback loop maps the topography of the sample surface where the effect of van der Waals interactions dominates. Since the magnetic forces are long ranged as compared to the van der Waals forces, the effect of the topographic variations can be eliminated to obtain a pure magnetic signal by lifting the tip to a certain height above the sample. For image processing, Gwyddion software [57] was used.

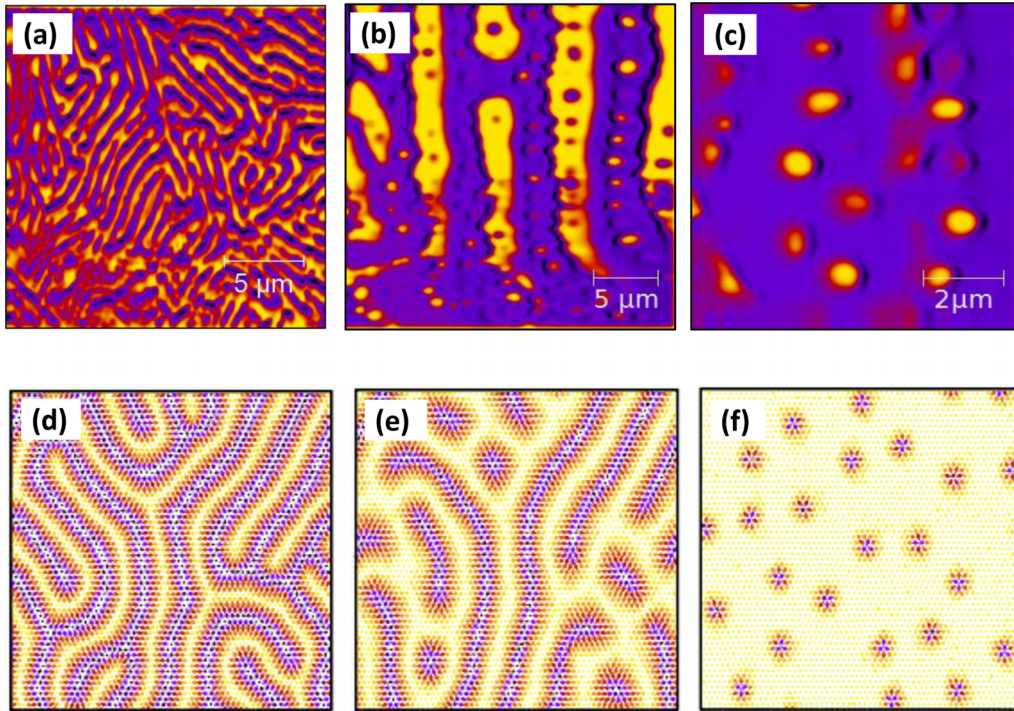


FIG. 3. MFM dual pass phase images taken on a cleaved single crystal of Fe_3GeTe_2 where (a) was taken at 1.6 K in the zero-field cooled (ZFC) state. The filamentary domains can be seen clearly. (b)–(c) were imaged in the field-cooled state in the presence of the field of the MFM cantilever. Representative spin configurations at $T/t = 0.01$ and $\lambda/t = 0.5$ for (d) $h_z = 0.2$, (e) $h_z = 0.44$, and (f) $h_z = 0.84$. The color bar corresponds to the z component, and the arrows indicate the planar components of the spins.

At 1.6 K, under zero-field cooled (ZFC) condition, we found filamentary domains with a typical domain width of around 900 nm as shown in Fig. 3(a). The domain structure involves stripes and interconnects with striking similarities with the computationally obtained filamentary domains as shown in Fig. 1(b). Note that the domain width obtained in simulations is much smaller compared to what is observed in Fe_3GeTe_2 (FGT). However, we explicitly verify that simulations on larger lattices with smaller λ lead to wider domains as shown in Fig. 4. Therefore, the mechanism of the formation of such domains is correctly captured within our approach. It is important to note that, unlike stripe domains [58] which consist of wide, parallel stripes of alternating magnetic

orientations, or fractal domains [59,60] which exhibit intricate and irregular patterns, filamentary domain wall structures are characterized by their continuous nature. In certain magnetic materials, especially those with strong magnetic anisotropy and competing interactions, the formation of filamentary domain wall structures can be energetically favorable.

In order to gain a further understanding of the magnetic state of Fe_3GeTe_2 , we performed MFM imaging in the field-cooled (FC) states of the crystal. We first field cooled the crystal under the magnetic field of the MFM cantilever and then performed MFM imaging at 1.6 K. Under this condition, as shown in Fig. 3(b), we found that circular domains (the dark circles) have formed within the stripes with the magnetization pointing opposite to the direction of the tip magnetization, along with rows of circular domains with the magnetization aligned in the opposite direction (the bright circles). This feature was reported earlier in Fe_3GeTe_2 and was related to high perpendicular magnetic anisotropy [61,62]. Interestingly, at several points, under the field, the stripes have also started breaking up into fragments. To investigate the microscopic structure in further detail, we imaged a smaller area [see Fig. 3(c)] under the same condition where we find an assembly of bright circular domains with a background hosting the fragmented stripes. Though the circular domains have a close resemblance with typical Skyrmions, their size is relatively larger ($\sim 500 \text{ nm}$) and may be called “magnetic bubbles.” These differ from the calculated domain structures within our model. In the model, the zero-field cooled protocol was followed with the temperature reduced to $T/t = 0.01$ in the absence of a magnetic field followed by the increase of field

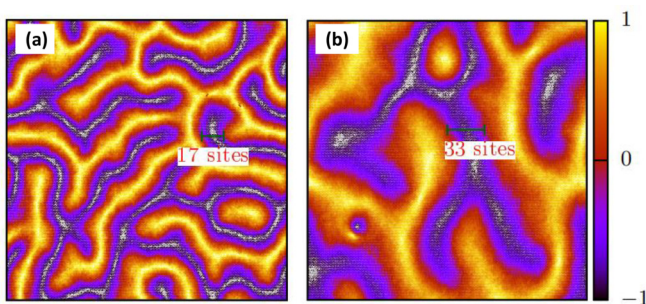


FIG. 4. Real-space view of spin configurations in $N = 240^2$ system at (a) $T/t = 0.01$ and $\lambda/t = 0.1$, and (b) $T/t = 0.005$ and $\lambda/t = 0.05$. The color bar corresponds to the z component, and the arrows indicate the planar components of the spins.

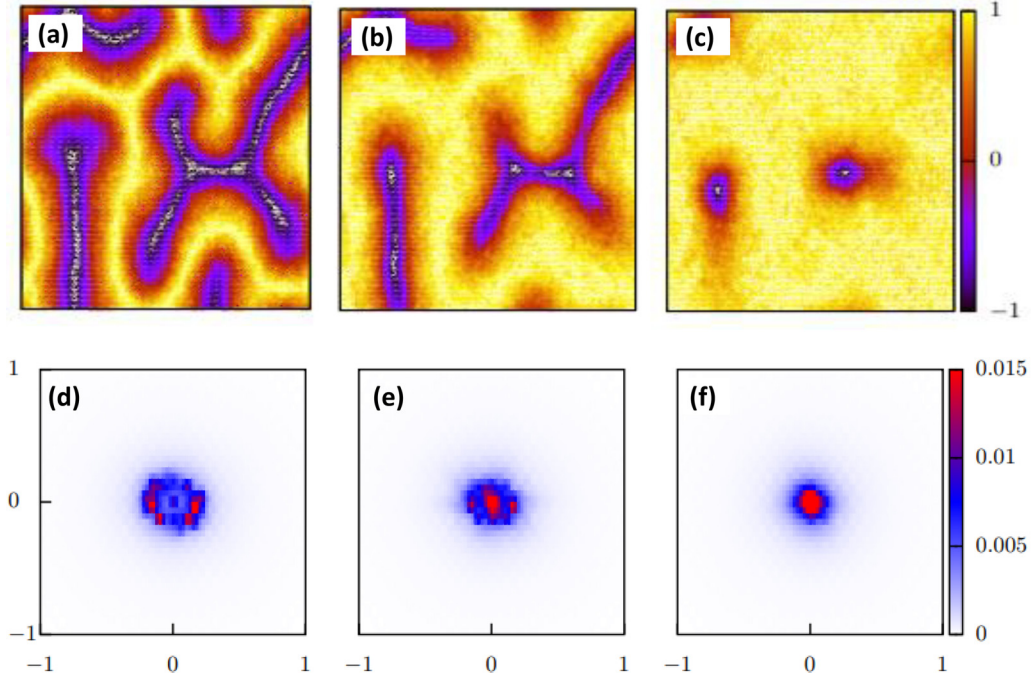


FIG. 5. Representative spin configurations at $T/t = 0.01$ and $\lambda/t = 0.1$ for (a) $h_z = 0.008$, (b) $h_z = 0.024$, and (c) $h_z = 0.032$. The color bar corresponds to the z component, and the arrows indicate the planar components of the spins. (d)–(f) The corresponding spin-structure factor for the three values of the magnetic field h_z .

in a step-wise manner until a fully saturated ferromagnetic state is obtained. Within the model, for intermediate values of the SOC strength, which is relevant for Fe_3GeTe_2 as noted earlier, the filamentary domains are seen to gradually break into well-defined Skyrmions upon increasing the magnetic field strength [see Figs. 3(d)–3(f)].

For small SOC, the filamentary domains are wide and the presence of a magnetic field leads to the generation of isolated large Skyrmions [see Figs. 5(a)–5(c)]. The typical size of skyrmions obtained here can be estimated from the inverse of the radius of the circular pattern in SSF [see Figs. 5(d)–5(e)]. Since the Skyrmions do not form any pattern, their presence is difficult to infer from the SSF. Indeed, the SSF shown in Fig. 5(f) indicates a ferromagnetic phase via a single peak at the Γ point. For strong SOC, the zero-field state is three-fold degenerate stripe state. This leads to the formation of a densely packed hexagonal pattern of Skyrmions at finite fields [see Figs. 6(a)–6(c)]. As expected, the SSF [Figs. 6(d)–6(f)] is more useful for identifying the formation of Skyrmions in this case as they organize into a lattice. The physics in the formation of filamentary domains in different SOC limit is similar, except for the domain width. In search for a deeper understanding of the difference between the experiment and the model, we studied the effect of a higher external field. For that, the crystal was first warmed up to 300 K and was then field cooled under an applied magnetic field of 1.2 kOe. Subsequently, the magnetic domains were imaged at zero applied field. As shown in Fig. 7(a), in a given area, we found that the stripes of bright domains with circular dark regions have broken into parts and formed individual circular domains with darker central region with brighter perimeters. There are regions where two such domains are seen to be connected where the breaking-up process remained incomplete. While

such circular domains are in majority, flat bright domains are also seen in the same region. In another region, where the surface is slightly tilted with respect to the MFM tip, the domains were imaged from an oblique direction which revealed a conical-like shape of the domains [see Fig. 7(b)]. This means, in Fig. 7(d), the ringlike domains are merely the top view of such conical-shaped domains. We then moved to an area where the bright flat domains are more in number, in order to investigate the distribution of their size and shape. As shown in Fig. 7(c), the flat domains appear to be fragments of the stripes in Fig. 3(a). The domains have condensed into different shapes including nearly circular and elongated ones. All these observations differed significantly from the results of the model [see Figs. 3(d)–3(f)].

IV. ROLE OF EASY-AXIS ANISOTROPY

To account for the discrepancy discussed above, we note that the model discussed so far does not include an important feature of the material, i.e., the presence of easy-axis anisotropy. It is important to ask if the presence of easy-axis anisotropy can explain the presence of large ferromagnetic bubbles in Fe_3GeTe_2 and the domain structure at higher magnetic fields. In order to investigate this, we included an additional term $-A_u \sum_i (S_i^z)^2$ in the Hamiltonian Eq. (4). Positive values of A_u represent an easy-axis scenario relevant to the material. The correspondence between the magnetic field values used in the experiment and the simulations is an important one, and the best way to compare the parameters is to compare the M/M_{sat} ratio at the applied field values. We find that $M/M_{\text{sat}} \approx 0.2$ at 1.2 kOe. For $h_z = 0.028$ [corresponding to Fig. 7(c)], we find $M/M_{\text{sat}} = 0.15$. Furthermore, the value of anisotropy parameter $A_u = 0.08$ used in the

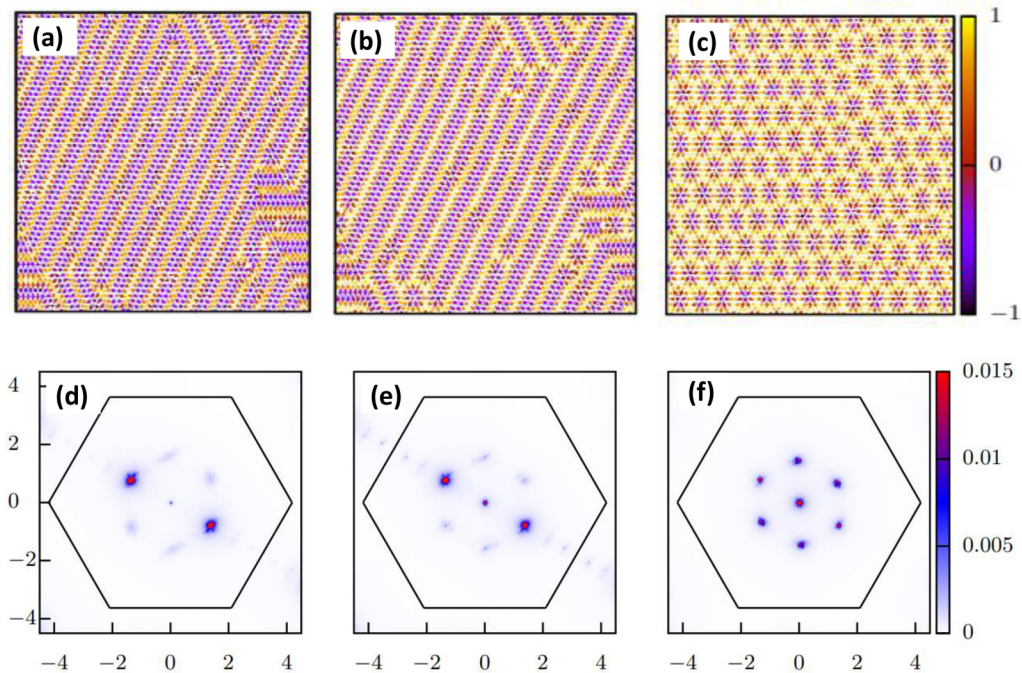


FIG. 6. Representative spin configurations at $T/t = 0.01$ and $\lambda/t = 1$ for (a) $h_z = 0.4$, (b) $h_z = 1.0$, and (c) $h_z = 1.4$. The color bar corresponds to the z component, and the arrows indicate the planar components of the spins. (d)–(f) The corresponding spin-structure factor for the three values of the magnetic field h_z .

simulations can be justified by comparing the ratio of the value of magnetization with the applied field oriented along the c axis to that oriented perpendicular to the c axis. We find that for the values of magnetic fields mentioned above,

$M_z(h||z)/M_x(h||x) \approx 3$ in experiments [56] as well as the simulations.

We find that the anisotropy scale competes with the Dzyaloshinskii-Moriya (DM) terms and therefore, the

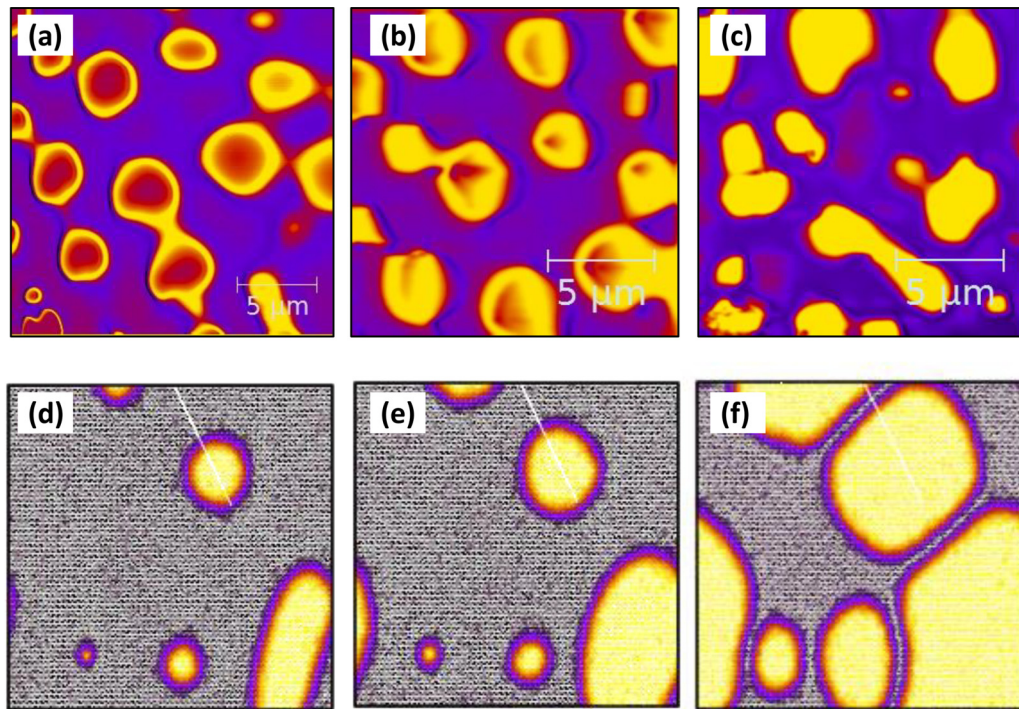


FIG. 7. (a)–(c) MFM dual pass images, recorded at different regions on the sample surface, in the field-cooled state (FC) where an external field of 1.2 kOe was applied. The lift height was kept constant at 30 nm for all the images. Representative spin configurations at $T/t = 0.01$, $\lambda/t = 0.1$, and $A_u = 0.08$ for (d) $h_z = 0.004$, (e) $h_z = 0.016$, and (f) $h_z = 0.028$.

tendency of spins to continuously tilt away from the single Skyrmion-core spin is suppressed. This leads to an expansion of the Skyrmion core and finite regions with ferromagnetic bubble character are stabilized [see Figs. 7(d)–7(f)]. These are consistent with the larger size “magnetic bubbles” that were seen experimentally under the field of the cantilever. Further, in the model, we find that upon increasing magnetic field strength the FM regions grow in size while remaining trapped inside self-enclosing domain walls. These are similar to the ringlike domain structures seen at 1.2 kOe. At even higher magnetic fields the model generates larger-size flat regions that show striking similarities with the flat regions seen experimentally. The variation of the experimental domain structure from point to point could be attributed to an inhomogeneity of the surface properties which might arise from an inhomogeneous distribution of the Fe vacancies in the system. Therefore, the results obtained in the simulations including an easy-axis anisotropy are now consistent with the evolution of the MFM images with applied magnetic field.

V. CONCLUSION

In conclusion, motivated by the demonstration of metallicity as well as ferromagnetism in the 2D materials Fe_nGeTe_2 ($n \geq 3$), we developed a model to understand the origin and the nature of topologically stable magnetic textures in a class of itinerant magnets. The model is generally applicable to spin-orbit coupled systems that display itinerant magnetism. Results of Monte Carlo simulations on our model display agreement with our experimental data on Fe_3GeTe_2 in identifying filamentary domain walls as the ground-state structure in the absence of magnetic field. In the presence of magnetic field the model

predicts either isolated Skyrmions or Skyrmion lattice, depending on the strength of the SOC. Our MFM experiments, on the other hand, reveal large-size magnetic bubbles with certain additional features. These magnetic structures were understood within the model when an easy-axis anisotropy term, as relevant to the materials under discussion, was included.

Our combined experimental and theoretical investigation on a class of vdW itinerant magnets has allowed us to identify easy-axis anisotropy as an important parameter that can tune the nature of topological textures from Skyrmions to magnetic bubbles. This generalization of Skyrmion-like topological textures establishes a conceptually new framework for characterizing real-space imaging data of experiments on itinerant magnets.

ACKNOWLEDGMENTS

G.S. acknowledges financial assistance from the Science and Engineering Research Board (SERB), Government of India (Grant No. CRG/2021/006395). G.S. also acknowledges S. N. Bose National Center for Basic Sciences, Kolkata, for faculty fellowship. D.R. and M.B. thank Department of Science and Technology (DST), Government of India for INSPIRE Fellowship. We acknowledge the use of the computing facility at IISER Mohali. R.R.C. acknowledges Department of Science and Technology (DST), Government of India, for financial support (Grant No. DST/INSPIRE/04/2018/001755) R.P.S. acknowledges the Science and Engineering Research Board (SERB), Government of India, for Core Research Grant No. CRG/2019/001028.

-
- [1] A. Fert, N. Reyren, and V. Cros, Magnetic skyrmions: advances in physics and potential applications, *Nat. Rev. Mater.* **2**, 17031 (2017).
 - [2] N. J. Laurita, G. G. Marcus, B. A. Trump, J. Kinder-vater, M. B. Stone, T. M. McQueen, C. L. Broholm, and N. P. Armitage, Low-energy magnon dynamics and magneto-optics of the skyrmionic Mott insulator Cu_2OSeO_3 , *Phys. Rev. B* **95**, 235155 (2017).
 - [3] R. Wiesendanger, Nanoscale magnetic skyrmions in metallic films and multilayers: a new twist for spintronics, *Nat. Rev. Mater.* **1**, 16044 (2016).
 - [4] A. Fert, V. Cros, and J. Sampaio, Skyrmions on the track, *Nat. Nanotechnol.* **8**, 152 (2013).
 - [5] N. Nagaosa and Y. Tokura, Topological properties and dynamics of magnetic skyrmions, *Nat. Nanotechnol.* **8**, 899 (2013).
 - [6] B. Göbel, A. Mook, J. Henk, and I. Mertig, Overcoming the speed limit in skyrmion racetrack devices by suppressing the skyrmion Hall effect, *Phys. Rev. B* **99**, 020405(R) (2019).
 - [7] K. Karube, K. Shibata, J. S. White, T. Koretsune, X. Z. Yu, Y. Tokunaga, H. M. Rønnow, R. Arita, T. Arima, Y. Tokura, and Y. Taguchi, Controlling the helicity of magnetic skyrmions in a β -Mn-type high-temperature chiral magnet, *Phys. Rev. B* **98**, 155120 (2018).
 - [8] A. N. Bogdanov and C. Panagopoulos, The emergence of magnetic skyrmions, *Phys. Today* **73**(3), 44 (2020).
 - [9] B. Dupe, M. Hoffmann, C. Paillard, and S. Heinze, Tailoring magnetic skyrmions in ultra-thin transition metal films, *Nat. Commun.* **5**, 4030 (2014).
 - [10] S. D. Pollard, J. A. Garlow, J. Yu, Z. Wang, Y. Zhu, and H. Yang, Observation of stable Néel skyrmions in cobalt/palladium multilayers with Lorentz transmission electron microscopy, *Nat. Commun.* **8**, 14761 (2017).
 - [11] N. Romming, C. Hanneken, M. Menzel, J. E. Bickel, B. Wolter, K. von Bergmann, A. Kubetzka, and R. Wiesendanger, Writing and deleting single magnetic skyrmions, *Science* **341**, 636 (2013).
 - [12] X. Z. Yu, N. Kanazawa, W. Z. Zhang, T. Nagai, T. Hara, K. Kimoto, Y. Matsui, Y. Onose, and Y. Tokura, Skyrmion flow near room temperature in an ultralow current density, *Nat. Commun.* **3**, 988 (2012).
 - [13] X. Zhao, C. Jin, C. Wang, H. Du, J. Zang, M. Tian, R. Che, and Y. Zhang, Direct imaging of magnetic field-driven transitions of skyrmion cluster states in FeGe nanodisks, *Proc. Natl. Acad. Sci. USA* **113**, 4918 (2016).
 - [14] S. Meyer, M. Perini, S. von Malottki, A. Kubetzka, R. Wiesendanger, K. von Bergmann, and S. Heinze, Isolated zero

- field sub-10 nm skyrmions in ultrathin Co films, *Nat. Commun.* **10**, 3823 (2019).
- [15] A. Tonomura, X. Yu, K. Yanagisawa, T. Matsuda, Y. Onose, N. Kanazawa, H. S. Park, and Y. Tokura, Real-space observation of skyrmion lattice in helimagnet MnSi thin samples, *Nano Lett.* **12**, 1673 (2012).
- [16] K. Karube, J. S. White, D. Morikawa, C. D. Dewhurst, R. Cubitt, A. Kikkawa, X. Yu, Y. Tokunaga, T.-h. Arima, H. M. Rønnow, Y. Tokura, and Y. Taguchi, Disordered skyrmion phase stabilized by magnetic frustration in a chiral magnet, *Sci. Adv.* **4**, eaar7043 (2018).
- [17] M. Hirschberger, T. Nakajima, S. Gao, L. Peng, A. Kikkawa, T. Kurumaji, M. Kriener, Y. Yamasaki, H. Sagayama, H. Nakao, K. Ohishi, K. Kakurai, Y. Taguchi, X. Yu, T.-h. Arima, and Y. Tokura, Skyrmion phase and competing magnetic orders on a breathing kagomé lattice, *Nat. Commun.* **10**, 5831 (2019).
- [18] C. Jin, Z.-A. Li, A. Kovacs, J. Caron, F. Zheng, F. N. Rybakov, N. S. Kiselev, H. Du, S. Blugel, M. Tian, Y. Zhang, M. Farle, and R. E. Dunin-Borkowski, Control of morphology and formation of highly geometrically confined magnetic skyrmions, *Nat. Commun.* **8**, 15569 (2017).
- [19] K. Karube, J. S. White, N. Reynolds, J. L. Gavilano, H. Oike, A. Kikkawa, F. Kagawa, Y. Tokunaga, H. M. Rønnow, Y. Tokura, and Y. Taguchi, Robust metastable skyrmions and their triangular-square lattice structural transition in a high-temperature chiral magnet, *Nat. Mater.* **15**, 1237 (2016).
- [20] K. M. Song, J.-S. Jeong, B. Pan, X. Zhang, J. Xia, S. Cha, T.-E. Park, K. Kim, S. Finizio, J. Raabe, J. Chang, Y. Zhou, W. Zhao, W. Kang, H. Ju, and S. Woo, Skyrmion-based artificial synapses for neuromorphic computing, *Nat. Electron.* **3**, 148 (2020).
- [21] J. Sampaio, V. Cros, S. Rohart, A. Thiaville, and A. Fert, Nucleation, stability and current-induced motion of isolated magnetic skyrmions in nanostructures, *Nat. Nanotechnol.* **8**, 839 (2013).
- [22] B. Ding, Z. Li, G. Xu, H. Li, Z. Hou, E. Liu, X. Xi, F. Xu, Y. Yao, and W. Wang, Observation of magnetic skyrmion bubbles in a van der Waals ferromagnet Fe₃GeTe₂, *Nano Lett.* **20**, 868 (2019).
- [23] M.-G. Han, J. A. Garlow, Y. Liu, H. Zhang, J. Li, D. Di-Marzio, M. W. Knight, C. Petrovic, D. Jariwala, and Y. Zhu, Topological magnetic-spin textures in two-dimensional van der Waals Cr₂Ge₂Te₆, *Nano Lett.* **19**, 7859 (2019).
- [24] P. Zhang, A. Das, E. Barts, M. Azhar, L. Si, K. Held, M. Mostovoy, and T. Banerjee, Robust skyrmion-bubble textures in SrRuO₃ thin films stabilized by magnetic anisotropy, *Phys. Rev. Res.* **2**, 032026(R) (2020).
- [25] C. Back, V. Cros, H. Ebert, K. Everschor-Sitte, A. Fert, M. Garst, T. Ma, S. Mankovsky, T. Monchesky, M. Mostovoy *et al.*, The 2020 skyrmionics roadmap, *J. Phys. D: Appl. Phys.* **53**, 363001 (2020).
- [26] S. M. Stishov, A. E. Petrova, S. Khasanov, G. K. Panova, A. A. Shikov, J. C. Lashley, D. Wu, and T. A. Lograsso, Magnetic phase transition in the itinerant helimagnet MnSi: Thermodynamic and transport properties, *Phys. Rev. B* **76**, 052405 (2007).
- [27] A. K. Nayak, V. Kumar, T. Ma, P. Werner, E. Pippel, R. Sahoo, F. Damay, U. K. Robler, C. Felser, and S. S. P. Parkin, Magnetic antiskyrmions above room temperature in tetragonal Heusler materials, *Nature (London)* **548**, 561 (2017).
- [28] C. Pfleiderer, D. Reznik, L. Pintschovius, H. v. Löhneysen, M. Garst, and A. Rosch, Partial order in the non-Fermi-liquid phase of MnSi, *Nature (London)* **427**, 227 (2004).
- [29] J. Jena, B. Gobel, T. Ma, V. Kumar, R. Saha, I. Mertig, C. Felser, and S. S. P. Parkin, Elliptical Bloch skyrmion chiral twins in an antiskyrmion system, *Nat. Commun.* **11**, 1115 (2020).
- [30] P.-J. Hsu, L. Rozsa, A. Finco, L. Schmidt, K. Palotas, E. Vedmedenko, L. Udvardi, L. Szunyogh, A. Kubetzka, K. von Bergmann, and R. Wiesendanger, Inducing skyrmions in ultrathin Fe films by hydrogen exposure, *Nat. Commun.* **9**, 1571 (2018).
- [31] S. X. Huang and C. L. Chien, Extended skyrmion phase in epitaxial FeGe(111) thin films, *Phys. Rev. Lett.* **108**, 267201 (2012).
- [32] X. Z. Yu, W. Koshibae, Y. Tokunaga, K. Shibata, Y. Taguchi, N. Nagaosa, and Y. Tokura, Transformation between meron and skyrmion topological spin textures in a chiral magnet, *Nature (London)* **564**, 95 (2018).
- [33] T. Nagase, M. Komatsu, Y. G. So, T. Ishida, H. Yoshida, Y. Kawaguchi, Y. Tanaka, K. Saitoh, N. Ikarashi, M. Kuwahara, and M. Nagao, Smectic liquid-crystalline structure of skyrmions in chiral magnet Co_{8.5}Zn_{7.5}Mn₄(110) thin film, *Phys. Rev. Lett.* **123**, 137203 (2019).
- [34] U. K. Robler, A. N. Bogdanov, and C. Pfleiderer, Spontaneous skyrmion ground states in magnetic metals, *Nature (London)* **442**, 797 (2006).
- [35] J. P. Chen, D.-W. Zhang, and J. M. Liu, Exotic skyrmion crystals in chiral magnets with compass anisotropy, *Sci. Rep.* **6**, 29126 (2016).
- [36] N. Mohanta, E. Dagotto, and S. Okamoto, Topological Hall effect and emergent skyrmion crystal at manganite-iridate oxide interfaces, *Phys. Rev. B* **100**, 064429 (2019).
- [37] S. D. Yi, S. Onoda, N. Nagaosa, and J. H. Han, Skyrmions and anomalous Hall effect in a Dzyaloshinskii-Moriya spiral magnet, *Phys. Rev. B* **80**, 054416 (2009).
- [38] J. Zang, M. Mostovoy, J. H. Han, and N. Nagaosa, Dynamics of skyrmion crystals in metallic thin films, *Phys. Rev. Lett.* **107**, 136804 (2011).
- [39] J. Iwasaki, A. J. Beekman, and N. Nagaosa, Theory of magnon-skyrmion scattering in chiral magnets, *Phys. Rev. B* **89**, 064412 (2014).
- [40] D. S. Kathyat, A. Mukherjee, and S. Kumar, Microscopic magnetic Hamiltonian for exotic spin textures in metals, *Phys. Rev. B* **102**, 075106 (2020).
- [41] D. S. Kathyat, A. Mukherjee, and S. Kumar, Antiskyrmions and Bloch skyrmions in magnetic Dresselhaus metals, *Phys. Rev. B* **104**, 184434 (2021).
- [42] S. Hayami and Y. Motome, Néel- and Bloch-type magnetic vortices in Rashba metals, *Phys. Rev. Lett.* **121**, 137202 (2018).
- [43] A. V. Bezvershenko, A. K. Kolezhuk, and B. A. Ivanov, Skyrmion-skyrmion interaction induced by itinerant electrons in a ferromagnetic strip, *Phys. Rev. B* **97**, 054408 (2018).
- [44] H. L. Zhuang, P. Kent, and R. G. Hennig, Strong anisotropy and magnetostriction in the two-dimensional Stoner ferromagnet Fe₃GeTe₂, *Phys. Rev. B* **93**, 134407 (2016).
- [45] J. Seo, D. Y. Kim, E. S. An, K. Kim, G.-Y. Kim, S.-Y. Hwang, D. W. Kim, B. G. Jang, H. Kim, G. Eom *et al.*, Nearly room temperature ferromagnetism in a magnetic metal-rich van der Waals metal, *Sci. Adv.* **6**, eaay8912 (2020).
- [46] A. F. May, D. Ovchinnikov, Q. Zheng, R. Hermann, S. Calder, B. Huang, Z. Fei, Y. Liu, X. Xu, and M. A. McGuire, Ferromagnetism near room temperature in the cleavable van der Waals crystal Fe₃GeTe₂, *ACS Nano* **13**, 4436 (2019).

- [47] Y. Wu, B. Francisco, Z. Chen, W. Wang, Y. Zhang, C. Wan, X. Han, H. Chi, Y. Hou, A. Lodesani *et al.*, A van der Waals interface hosting two groups of magnetic skyrmions, *Adv. Mater.* **34**, 2110583 (2022).
- [48] C. A. Akosa, H. Li, G. Tataru, and O. A. Tretiakov, Tuning the skyrmion Hall effect via engineering of spin-orbit interaction, *Phys. Rev. Appl.* **12**, 054032 (2019).
- [49] Y. You, Y. Gong, H. Li, Z. Li, M. Zhu, J. Tang, E. Liu, Y. Yao, G. Xu, F. Xu *et al.*, Angular dependence of the topological Hall effect in the uniaxial van der Waals ferromagnet Fe_3GeTe_2 , *Phys. Rev. B* **100**, 134441 (2019).
- [50] Y. Wang, J. Yan, J. Li, S. Wang, M. Song, J. Song, Z. Li, K. Chen, Y. Qin, L. Ling *et al.*, Magnetic anisotropy and topological Hall effect in the trigonal chromium tellurides Cr_5Te_8 , *Phys. Rev. B* **100**, 024434 (2019).
- [51] S. Kumar and P. Majumdar, A travelling cluster approximation for lattice fermions strongly coupled to classical degrees of freedom, *Eur. Phys. J. B* **46**, 315 (2005).
- [52] M. Birch, L. Powalla, S. Wintz, O. Hovorka, K. Litzius, J. Loudon, L. Turnbull, V. Nehruji, K. Son, C. Bubeck *et al.*, History-dependent domain and skyrmion formation in 2D van der Waals magnet Fe_3GeTe_2 , *Nat. Commun.* **13**, 3035 (2022).
- [53] H.-J. Deiseroth, K. Aleksandrov, C. Reiner, L. Kienle, and R. K. Kremer, Fe_3GeTe_2 and Ni_3GeTe_2 - Two new layered transition-metal compounds: Crystal structures, HRTEM investigations, and magnetic and electrical properties, *Eur. J. Inorg. Chem.* **2006**, 1561 (2006).
- [54] K. Kim, J. Seo, E. Lee, K.-T. Ko, B. Kim, B. G. Jang, J. M. Ok, J. Lee, Y. J. Jo, W. Kang *et al.*, Large anomalous Hall current induced by topological nodal lines in a ferromagnetic van der Waals semimetal, *Nat. Mater.* **17**, 794 (2018).
- [55] B. Chen, J. Yang, H. Wang, M. Imai, H. Ohta, C. Michioka, K. Yoshimura, and M. Fang, Magnetic properties of layered itinerant electron ferromagnet Fe_3GeTe_2 , *J. Phys. Soc. Japan* **82**, 124711 (2013).
- [56] R. R. Chowdhury, S. DuttaGupta, C. Patra, O. A. Tretiakov, S. Sharma, S. Fukami, H. Ohno, and R. P. Singh, Unconventional Hall effect and its variation with Co-doping in van der Waals Fe_3GeTe_2 , *Sci. Rep.* **11**, 14121 (2021).
- [57] D. Nečas and P. Klapetek, Gwyddion: an open-source software for SPM data analysis, *Centr. Eur. J. Phys.* **10**, 181 (2012).
- [58] S. Voltan, C. Cirillo, H. Snijders, K. Lahabi, A. Garcia Santiago, J. Hern'andez, C. Attanasio, and J. Aarts, Emergence of the stripe-domain phase in patterned permalloy films, *Phys. Rev. B* **94**, 094406 (2016).
- [59] A. Kreyssig, R. Prozorov, C. Dewhurst, P. Canfield, R. McCallum, and A. Goldman, Probing fractal magnetic domains on multiple length scales in $\text{Nd}_2\text{Fe}_{14}\text{B}$, *Phys. Rev. Lett.* **102**, 047204 (2009).
- [60] G. Catalan, H. Béa, S. Fusil, M. Bibes, P. Paruch, A. Barthelemy, and J. Scott, Fractal dimension and size scaling of domains in thin films of multiferroic BiFeO_3 , *Phys. Rev. Lett.* **100**, 027602 (2008).
- [61] G. D. Nguyen, J. Lee, T. Berlijn, Q. Zou, S. M. Hus, J. Park, Z. Gai, C. Lee, and A.-P. Li, Visualization and manipulation of magnetic domains in the quasi-two-dimensional material Fe_3GeTe_2 , *Phys. Rev. B* **97**, 014425 (2018).
- [62] N. Leon-Brito, E. D. Bauer, F. Ronning, J. D. Thompson, and R. Movshovich, Magnetic microstructure and magnetic properties of uniaxial itinerant ferromagnet Fe_3GeTe_2 , *J. Appl. Phys.* **120**, 083903 (2016).